Friction **10**(8): 1258–1275 (2022)
https://doi.org/10.1007/s40544-021-0553-x
ISSN 2223-7690
CN 10-1237/TH
RESEARCH ARTICLE

Load dependent microstructural evolution in an as-cast 26% Cr high chromium cast iron during unlubricated sliding

U. Pranav NAYAK[1, *], Sebastian SUÁREZ[1], Valentin PESNEL[3], Frank MÜCKLICH[1,2], María Agustina GUITAR[1]

[1] *Department of Materials Science, Saarland University, Saarbrücken 66123, Germany*

[2] *Materials Engineering Center Saarland, Saarbrücken 66123, Germany*

[3] *Ecole Européenne d'ingénieurs en Génie des Matériaux, Université de Lorraine, Nancy 54000, France*

Received: 12 April 2021 / Revised: 07 June 2021 / Accepted: 05 September 2021

Abstract: In the current study, an as-cast 26% Cr high chromium cast iron (HCCI) alloy was subjected to dry-sliding linear wear tests, under different loads. The loads were selected based on analytically computing the critical load (P_C) i.e., the load necessary to induce plastic deformation. The P_C was calculated to be 15 N and accordingly, a sub-critical load (5 N) and an over-critical load (20 N) were chosen. The influence of increasing the load during the wear test was investigated in terms of the matrix microstructural behaviour and its ability to support the surrounding carbides. The morphological aspects of the wear tracks, and the deformed matrix microstructure adjacent and underneath the track was analysed by confocal laser scanning microscope (CLSM) and scanning electron microscope (SEM), respectively. No evidence of plastic deformation of the matrix was observed below P_C. On the contrary, at loads equal to and higher than P_C, the austenitic matrix plastically deformed as evidenced by the presence of slip bands. Electron backscattered diffraction (EBSD) measurements in terms of grain reference orientation deviation, and micro-Vickers hardness of the austenitic matrix indicated a deformation depth of about 40 μm at the maximum applied load of 20 N. The active wear mechanisms during sliding were a combination of both adhesive and abrasive wear, although increasing the load shifted the dominant mechanism towards abrasion. This was primarily attributable to the increased propensity for carbide cracking and fracturing, combined with the inability of the hardened austenitic matrix surface and sub-surface to adequately support the broken carbide fragments. Moreover, the shift in the dominant wear mechanism was also reflected in the wear volume and subsequently, the wear rate.

Keywords: high chromium cast iron; unlubricated sliding; plastic deformation; wear resistance; carbide spallation; matrix hardness

1 Introduction

The ASTM A532 describes high chromium cast irons (HCCIs) as alloys containing 15–30 wt% Cr and 2.4–4 wt% C (with minor additions of Mn, Ni, Cu, and Mo), belonging to the Fe–Cr–C ternary system [1, 2]. They were created in the 1930's, with continuous improvements made over the years and are already being used in applications that demand excellent wear resistance and moderate toughness in coal and mineral industries [3]. Their applicability in ore crushers, ball mill liners, and pulverizing equipment is mainly due to the presence of hard, dispersed chromium-iron carbides, in the as-cast state. Moreover, combining the hard carbides with the relatively softer matrix surrounding it, and the overall associated cost, makes it an attractive choice to be used in these industries [4–7].

In HCCI alloys, increasing the Cr content will modify the type and nature of the eutectic carbides

* Corresponding author: U. Pranav NAYAK, E-mail: pranav.nayak@uni-saarland.de

(EC), from a continuous M_3C type to a discontinuous M_7C_3 type [8, 9]. Given the inherent brittleness associated with the carbide, continuous precipitates are not favoured for abrasion resistance and therefore, the discontinuous, and relatively tougher M_7C_3 carbides are advantageous [10]. The M_7C_3 hardness is about 1,200–1,600 HV depending on the chemical composition and the orientation, which, is much higher than austenitic or martensitic matrix structures encountered in hypoeutectic HCCI variants [11]. Additionally, the carbide volume fraction (CVF) and the orientation of the carbides influence the overall wear resistance [12, 13].

Several works focus on the influence of alloying and CVF on the final wear properties of the HCCI alloys, and studies are devoted to find the optimum CVF for a given chemical composition to obtain the maximum wear resistance [13–17]. Initially, the resistance to wear was thought to be mainly influenced by the hardness of the material, as empirically demonstrated by Archard [18]. It is now understood that a lot of factors contribute to the overall wear resistance, such as the carbide's type, morphology, volume fraction, and its interaction with the host matrix. Therefore, the overall wear resistance can be thought of a synergistic contribution between both the carbide and the matrix that surrounds it [19, 20].

Despite the crucial contribution of the hard M_7C_3 carbides in improving the overall wear resistance of the HCCI alloy, the degree of mechanical support provided by the matrix structure plays a pivotal role [21, 22]. This was evident in the study carried out by Doğan et al. [23], where the increase in the CVF did not necessarily increase the wear resistance in the examined HCCI alloys. Therefore, it can be said that the wear behaviour of a material is not an inherent property but is defined wholly by the system and in this regard, the carbides' hardness contributes partly to the wear resistance [24].

As far as the matrix structure is concerned, pearlitic and ferritic matrix is avoided as their presence will reduce both wear and fracture resistance [10, 25]. Austenite in general is thought to provide a better mechanical support for the carbides compared to pearlite/bainite due to its ability to absorb the crack propagation and strain harden progressively during service [26–28]. This was apparent in the work carried out by Doğan et al. [23], where it was observed that the HCCI with an austenitic matrix and CVF of 28% showed a decrease in the volume wear rate by almost 50% compared to the alloy with a pearlitic/bainitic matrix having a CVF of 45%.

It was shown in several studies that heat treatment modifications made to the as-cast HCCI alloy have improved the wear resistance [29–33]. On the other hand, there are studies which indicate that a harder martensitic matrix might not be the most optimal choice [23, 25]. Moreover, numerous studies indicate a tendency of increasing wear resistance with increasing CVF when an abrasive softer than the M_7C_3 carbide is used, although there is no consensus among the community when the hardness exceeds that of the carbide (SiO_2/Al_2O_3) [26, 34]. Thus, the wear behaviour is not only influenced by the microstructure of the HCCI alloy, but also by other factors such as the experimental environment, loading conditions, the relative movement of the contact surface, the abrasive type, and hardness [21]. This just elucidates the complexity and the variables associated with tribological testing.

Among a multitude of studies dealing with wear in cast irons, only a limited number of investigations dealt with sliding wear [21, 35, 36] and even fewer studies emphasised on the matrix modifications taking place during sliding [14, 24]. It is thought that in addition to the dislocation interactions, the formation of strain induced martensite (SIM) also contributes to the work hardening behaviour of austenite [37]. Although the transformation from austenite to martensite under abrasion is mentioned by Pokusová et al. [38], it is not described as such. The ability of the austenite matrix to plastically deform during service and its ability to form SIM gives scope for further improvement in creating a self-replacing wear resistance surface, increasing the longevity of the wear parts [10, 25].

In the current work, an attempt was made to investigate the microstructural evolution of an as-cast 26% Cr HCCI alloy under three different loading conditions during dry-sliding. The loads were selected after performing analytical calculations based on the materials' parameters using Hertzian contact theory. The wear tracks were subjected to confocal laser scanning microscopy (CLSM) and scanning electron

microscopy (SEM) to examine the morphological aspects of the tracks and ascertain the acting wear mechanisms. This was further complemented by performing electron backscattered diffraction (EBSD) measurements on the regions adjacent to, and underneath the wear tracks. Furthermore, quantification of wear, in terms of wear rate, and the coefficient of friction (COF) evolution with increasing loads, were assessed. In the current alloy, as the matrix is predominately austenitic, understanding its behaviour under the given tribological conditions will bolster the alloy's further development in applications involving sliding wear such as liner plates and vertical roller mill liners [5, 21].

2 Materials and methodology

The bulk chemical composition (in wt%) of the 26% Cr HCCI alloy was determined by optical emission spectroscopy (GNR Metal Lab 75/80; G.N.R. S.r.l., Agrate Conturbia, Novara, Italy) and is presented in Table 1. The specifics of the casting are mentioned in [39]. An abrasive disk was used to cut the cast samples measuring 20 mm × 20 mm × 10 mm and later, hot embedded using a conductive resin for microstructural characterization. Standard metallographic procedure was followed as detailed in Ref. [40], to obtain a scratch-free, mirror polished surface. The microstructure of the as-cast sample composed of M_7C_3 (~ 30%) (M: Cr, Fe) eutectic carbides (EC) dispersed in an austenitic matrix (γ) (~ 60%), and a thin layer of martensite (α') (~10%) sandwiched between the EC and γ, as depicted in Fig. 1(a). Further microstructural analyses, concerning the phase fraction and elemental composition has previously been carried out [39, 40]. The presence of

Table 1 Bulk chemical composition (wt%) of the HCCI alloy.

C	Cr	Mn	Ni	Mo	Si	Cu	P	S	Fe
2.53	26.60	0.66	0.26	0.24	0.37	0.03	<0.01	0.04	Bal.

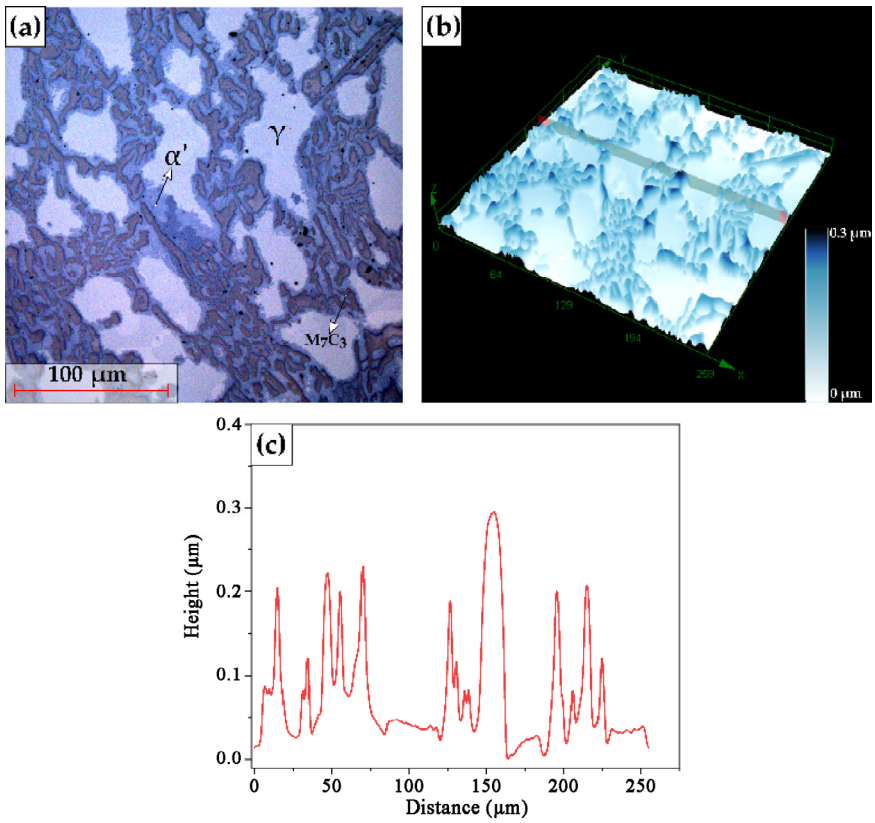

Fig. 1 (a) Representative CLSM micrograph of the as-cast HCCI sample in the unworn state, with the austenitic matrix (γ), M_7C_3 EC, and interfacial martensite (α') indicated; (b) 3D view of the topographical map along with the height range; and (c) height profile taken across the sample surface.

martensite between the γ–M_7C_3 interface is a common occurrence during the casting of HCCI alloys and is a well-documented phenomenon [9, 31, 41, 42].

Dry-sliding wear tests in a linear reciprocating motion were conducted using a ball-on-disc micro-tribometer (CSM Instruments), while the whole setup was placed in an environmental chamber to control the temperature and humidity. 3 mm alumina (Al_2O_3) balls (99.00%–99.99 % purity; Grade GD28) were used as the sliding counter-body. The roughness of the sample and balls was measured using a LEXT OLS 4100 Olympus CLSM (Olympus Corporation, Tokyo, Japan). The CLSM uses a laser with 405 nm wavelength and, a lateral and vertical resolution of 120 and 10 nm, respectively. Figure 1(b) depicts a 3D topographical map of Fig. 1(a), and Fig. 1(c) represents the height profile taken across the sample surface. It is worth to mention that height variation is a direct consequence of the difference in the removal rates between the matrix and carbide phase during metallographic preparation, owing to their dissimilar hardness. This is reflected in the sample roughness. The roughness, described by the root mean square (RMS) value, S_q, was 0.07 ± 0.01 μm for the sample, measured in an area of 650 μm × 650 μm. The ball roughness was 0.250 ± 0.05 μm. It should be noted that before commencement of the wear testing, the balls were rinsed in an ultrasonic bath separately with acetone and isopropanol for 10 minutes each.

The value of the critical load (P_C) i.e., the load at which the outset of plastic deformation takes place in the material, was determined applying the Hertzian contact theory, using Eqs. (1) and (2) [43, 44]. It should be noted that the values considered while carrying out these approximations are of the material that fails first. Since the matrix is the relatively softer phase compared to the M_7C_3 carbide, it will yield first. Hence, the P_C calculations were carried out by considering the properties of the alumina ball and the austenitic matrix.

$$P_c = \frac{4}{3}\left(\frac{R}{E'}\right)^2\left(\frac{C}{2}\pi \cdot S_y\right)^3 \quad (1)$$

$$\frac{1}{E'} = \frac{1-\nu_1^2}{E_1} + \frac{1-\nu_2^2}{E_2} \quad C = 1.295\exp(0.736\nu) \quad (2)$$

where P_C is the critical contact force at yielding (N), R is the radius of the alumina ball (m), E' is the equivalent elastic modulus (GPa), E_1 and E_2 represent the elastic modulus of the alumina ball and the austenitic matrix, respectively, ν_1 and ν_2 are the Poisson's ratio of the ball and the matrix, respectively, C is the yield strength coefficient and S_y is the yield strength of the matrix. The hardness (H) and Young's modulus (E) values of the austenitic matrix (in GPa) were obtained from nano-indentation measurements (Hysitron TI 900 TriboIndenter), using a Berkovich tip, with a tip depth of 200 nm used in displacement mode. A loading/unloading rate of 50 was maintained and the scan size was approximately 30 μm [39]. Each indentation time was 2 min, and the values were averaged over 25 readings. The S_y of the matrix was determined from the H using a variant of the Tabor relationship ($S_y = H/2.84$) [45]. The values of the parameters used in the Eqs. (1) and (2) are given in Table 2.

The P_C was found out to be ~ 15 N and accordingly, three loads (P), 5, 15, and 20 N, were chosen for the wear tests. Moreover, the specifics concerning the tribological testing parameters are given in Table 3. Three trials were performed for each load.

Table 2 Parameters used for the critical load calculations.

Parameter	Value
R (m)	1.50×10^{-3}
E_1 (Pa) [46]	3.65×10^{11}
E_2 (Pa)	2.38×10^{11}
ν_1 [47]	0.22
ν_2 [48]	0.28
E' (Pa)	1.54×10^{11}
H (Pa)	5.60×10^{9}
S_y (Pa)	1.97×10^{9}
C	1.5914

Table 3 Tribological testing parameters.

Parameter	Value
Temperature (°C)	25
Relative humidity (%)	45
Load (N)	5, 15, 20
Sliding velocity (m/s)	0.02
Stroke length (mm)	5.5
No. of cycles	2,000
Data acquisition frequency (Hz)	50

CLSM was used to analyse the evolution of the wear tracks with increasing load and the corresponding morphological aspects, whereas the fine microstructural details were observed using a FEI Helios Nanolab field emission scanning electron microscope (FE-SEM). The SEM was operated at an acceleration voltage of 5–15 kV and a beam current of 1.4 nA. Moreover, a high sensitivity backscattered electron detector (vCD) was used to obtain a better contrast between the phases. Energy-dispersive X-ray spectroscopy (EDS) was used to evaluate the chemical composition of the worn, and unaffected surfaces. Furthermore, to observe the deformed microstructure underneath the wear track and to prevent further modifications from the mechanical sectioning and polishing, the surface was electrolytically coated with Ni.

EBSD was used to investigate the local deformation and the strain distribution in the austenitic matrix, adjacent and beneath the wear track. The measurements were performed at an acceleration voltage of 20 kV and a beam current of 11 nA, using a field emission gun in the FE-SEM workstation equipped with an EDAX Hikari EBSD camera. Kernel average misorientation (KAM) measurements were carried out to extract orientation data within the deformed regions. Owing to the very small step size (30–50 nm), 2nd neighbour KAM with a 5° threshold was considered for the analysis. Additionally, grain reference orientation deviation (GROD) analysis was performed within the austenitic regions to obtain the orientational variation, with increasing cross-sectional depth. The EBSD data was analysed using the Orientation Imaging Microscopy (OIM™ v. 7) Data Analysis software by EDAX Inc.

Furthermore, the hardness of the austenitic matrix adjacent and underneath the wear track, was determined using the Vickers method. A Struers Dura Scan 50 microhardness tester (Struers Inc., Cleveland, OH, USA) with a load of 0.09807 N (HV 0.01) was used for this purpose. During the testing, the dwell time was 15 s and an average of 15–20 readings were considered. The load was chosen such that the surrounding entities are not participating in the evaluation of the matrix hardness and the indentation mark was clearly resolvable using the optical microscope.

Wear quantification was described in terms of wear rate, and it was proceeded by calculating the volume loss encountered in each track, using the LEXT software. The entire wear track, including the ends were considered in the calculations, and Eq. (3) was used to compute the wear rate. Similar variations of Eq. (3) were used in other studies to quantify wear, where mass loss and density had been considered [49–51]. In Eq. (3), V represents the wear volume (mm^3), l is the total sliding distance (5.5 × 2 × 2,000 mm), P is the applied load (N), and K represents the wear rate (mm^3/(N·mm)).

$$K = \frac{V}{l \times P} \tag{3}$$

3 Results and discussions

3.1 Microstructural characterization of the worn samples

Figures 2(a)–2(c) represent the CLSM micrographs of the sample surface with a 50% overlay of the height profile, for the increasing loads, after wear. The 'composite' CLSM micrograph was divided based on height (left-half) and intensity (right-half) to have a better visualization across the wear track. The height range (pertaining only to the height profile) and the sliding direction (SD) is also mentioned for reference. The variation in the height from the wear track edge towards the centre, with increasing load, can be clearly observed. The depth profile, taken across the wear track (as indicated by the horizontal red dashed line), is graphically represented in Fig. 2(d). Additionally, the wear width increased with increasing load, as shown in Fig. 2(e).

3.1.1 Sub-critical load (P = 5 N)

Figure 3 represents the SEM micrographs of the worn surface morphology after subjecting it to sliding at 5 N. Initially, as the Al_2O_3 ball traverses over the sample surface, some material transfer takes place owing to the high contact pressure established by the ball's asperities, causing adhesion [27, 52]. Furthermore, the reciprocating effect of sliding and the subsequent shearing action results in adhesive wear and the formation of wear debris as indicated in Fig. 3(a). A closer examination of the wear track in Fig. 3(b) reveals carbide micro-cracking, primarily perpendicular to the

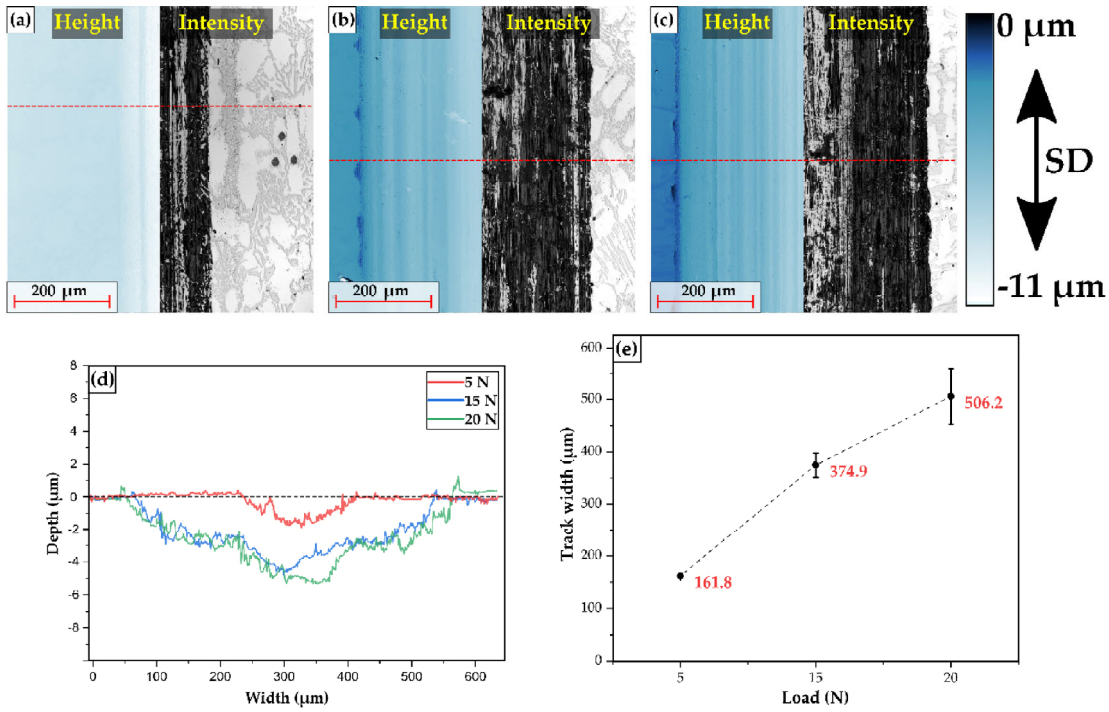

Fig. 2 CLSM micrographs of the wear tracks with a 50% overlay of the height profile for (a) 5 N, (b) 15 N, and (c) 20 N. The part of the CLSM micrograph based on height, and intensity is indicated within the micrograph for reference. The height range (pertaining only to the height profile) and the sliding direction (SD) is also mentioned. (d) Depth profile taken across the wear tracks for the different load as indicated by the horizontal red dashed line in the differently loaded micrographs. (e) Average wear track width for each load.

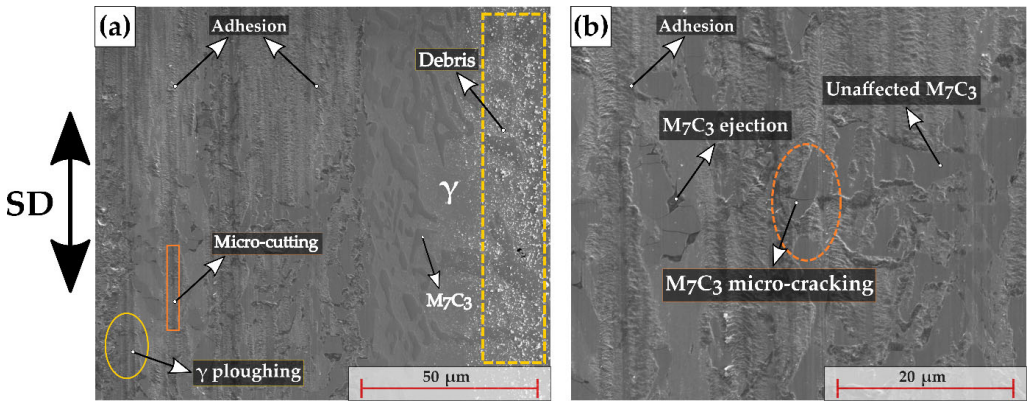

Fig. 3 (a) and (b) SEM micrographs in secondary electron (SE) mode of the wear track loaded at 5 N, with the various wear track aspects delineated within the micrograph. The austenitic matrix (γ) and the eutectic carbides (M_7C_3) are indicated in (a). The orange solid rectangle represents the micro-cutting phenomena whereas the orange dashed ellipse indicates the carbide micro-cracking. The wear debris generated is indicated by the yellow dashed rectangle whereas the yellow solid ellipse represents the ploughing of the austenitic matrix. The SD is also mentioned for reference.

sliding direction. Even though the load used currently is below P_C, given the higher hardness of the Al_2O_3 balls (~ HV 1,500) compared to the M_7C_3 carbides (~ HV 1,200), they are able to crack and fracture the carbides, in addition to affecting the matrix [10, 25]. The carbide cracking and fragmentation eventually leads to its ejection. The fractured carbides can then act as third-body entities, causing further grooving in the material, leading to the phenomenon of micro-cutting and micro-ploughing, characteristics of abrasive wear, as delineated in Fig. 3(a). It is also worth to note that the majority of M_7C_3 carbides were cracked, but not ejected from their position. This was attributable to the ductility of the austenitic matrix which provided

adequate mechanical support, preventing carbide spallation. Subsequently, it was concluded that the active wear mechanisms were adhesion with mild abrasion.

Although no evidence of plastic deformation of the austenitic matrix adjacent to the wear track was observed from the SEM micrographs, EBSD measurements indicated the sporadic presence of slip lines adjacent to the track, as seen in Fig. 4(a). Comparing the image quality (IQ) map (Fig. 4(a)) to the phase map (Fig. 4(b)), the slip lines were seen to be originating from the martensitic area adjacent to the wear track and not directly from the austenite. Hence, this can be thought more of a local deformation caused by the compressive nature of the hard martensite present in between the carbide and austenite, rather than a shear deformation induced by the ball. The material flow stemming from the wear testing, combined with the associated presence of martensite at the carbide–austenite interface could impart some compressive action leading to a slight local deformation, resulting in the occurrence of slip traces.

Figures 4(c) and 4(d) represent the IPF and KAM maps of the austenite matrix, respectively. KAM is basically the average misorientation between each pixel and the chosen neighbours. Increased misorientation indicates the accumulation of strain inside the material and it is used to study the sub-structures [53]. It is evident from both maps that no misorientation within the austenite matrix has occurred. Indeed, the misorientation at the periphery of the matrix is higher than the centre which can be attributable to the presence of the martensitic layer, engulfing and straining the matrix. However, it must also be noted that the uncertainty associated with filtering the artefacts at the edge boundaries can also play a role.

3.1.2 *Critical load (P = 15 N)*

The wear was conducted at the critical load, and the SEM micrographs depicting all the effects that resulted during the wear test are represented in Fig. 5. Similar to Fig. 3, characteristics of both adhesive and abrasive wear was seen on the wear tracks, as indicated in Fig. 5(a). Owing to the increased load, plastic deformation of the austenitic matrix adjacent to the wear track took place, as evidenced from the presence of slip traces, and predicted by the calculations. These slip traces are formed to accommodate the deformation endured by the austenitic matrix owing to the tangential forces exerted by the ball during the test [54]. Moreover, a second set of slip traces was revealed adjacent to the wear track, present closer to the martensite layer and can be visualised in Fig. 5(b). The second slip system activation could take place to accommodate the higher local deformation exerted by the shearing action of the ball and due to the increased local strain closer to the martensite layer. The carbide micro-cracking and ejection can be visualized in Fig. 5(c). It was observed that the proportion of the spalled carbides had increased compared to the wear testing under 5 N load, resulting in a shift in the active wear mechanism towards abrasive wear. Unlike the previous case, where the austenitic matrix was mainly undeformed, the increased load resulted in its plastic deformation rendering it unable to support the fractured carbides. This led to an increased occurrence of micro-cutting and micro-ploughing, as indicated by the orange solid rectangle and the yellow solid ellipse, respectively.

Furthermore, the difference in brightness between

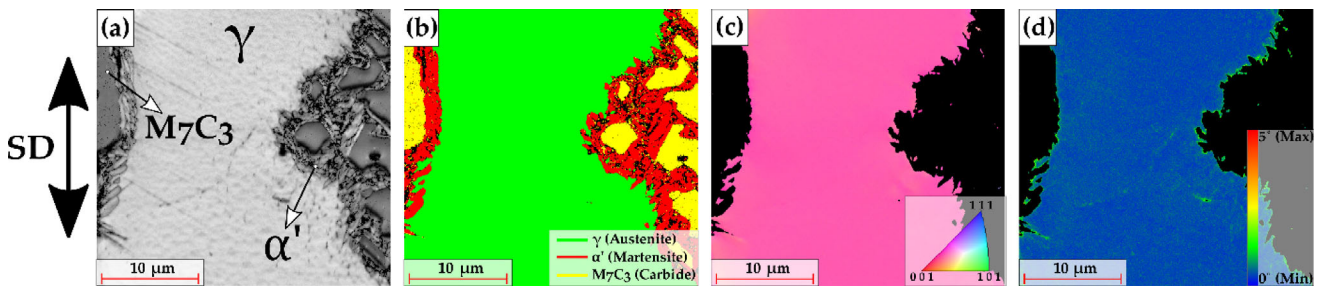

Fig. 4 EBSD measurements on the region adjacent to the 5 N track with (a) IQ map of the scanned region with the respective phases indicated, (b) phase map with the phases marked in different colours, (c) inverse pole figure (IPF) map of the austenite matrix, and (d) KAM map of the austenite matrix.

the deformed and the undeformed austenite, as observed in Fig. 5(d), stems from the orientational gradients during the plastic deformation. Additionally, the two different sets of slip traces are marked, as indicated in Fig. 5(e). The increased matrix hardening associated with the higher load combined with the increased propensity for carbide cracking, could prove detrimental to the overall wear behaviour of the alloy. This is evident in Fig. 5(a) where the carbides have been cracked and removed, resulting in the formation of debris, and as seen further, wear loss. Hence, it was concluded that the active wear mechanism had shifted from a primarily adhesive wear with mild abrasion, to an abrasion-dominated wear with signs of mild adhesion in the track.

Analogous to the 5 N wear track, EBSD analysis was performed on the 15 N track, with particular emphasis being placed on the austenite matrix adjacent to the wear track. The influence of using a higher load can be acknowledged. It seems that the slip lines terminate as they reach the martensite phase, as depicted in Fig. 6(a), which can be attributed to the difference in the crystal structure and higher hardness. The IPF map of the austenite matrix, in Fig. 6(c), indicates a variance in the crystal orientation especially at regions where the two sets of slip lines intersect. The same can be visualized from the KAM map, in Fig. 6(d), wherein a higher misorientation is present where the intersection of the slip lines takes place.

3.1.3 *Over-critical load (P = 20 N)*

Finally, wear testing at 20 N was carried out and the SEM micrographs of the wear track in BSE mode are shown in Fig. 7. It was observed from Figs. 7(a)

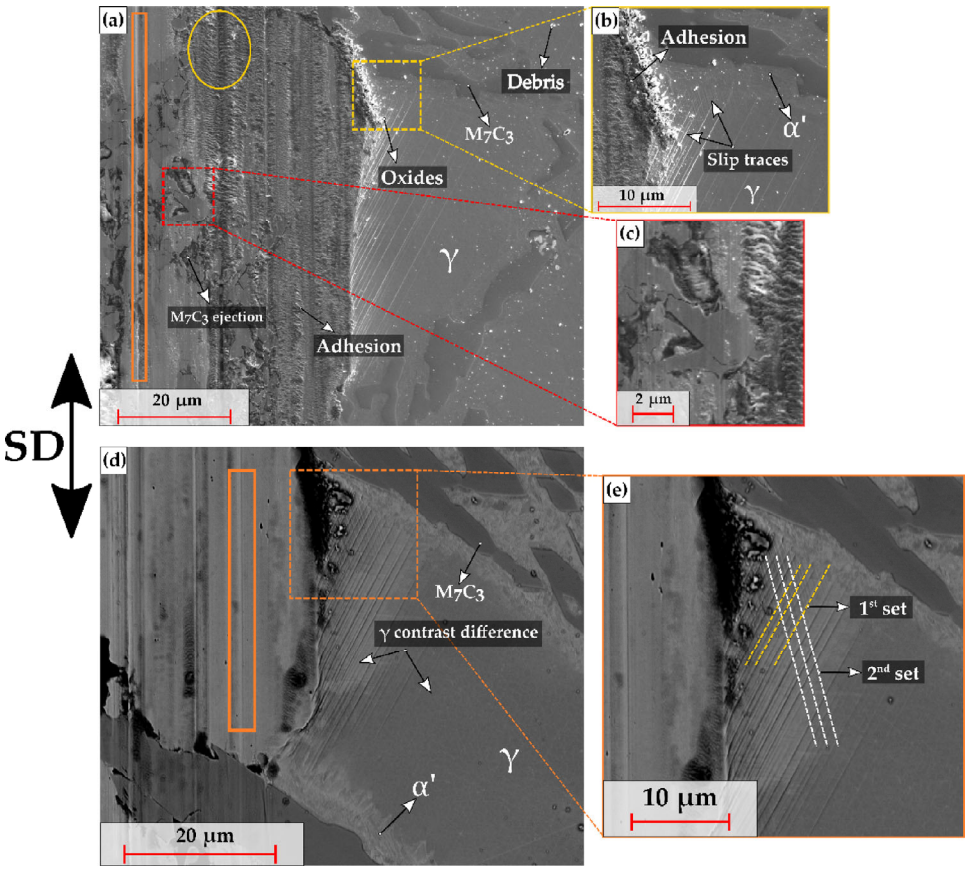

Fig. 5 (a) SEM micrograph in SE mode of the wear track loaded at 15 N, with the austenitic matrix (γ), M_7C_3 carbides, oxides, and the wear debris delineated within the micrograph. The presence of slip traces along with the martensite phase (α'), and the phenomenon of adhesion is indicated in (b) whereas, the partially cracked and removed carbide is observed in (c). The orange solid rectangle represents the micro-cutting phenomena, and the yellow solid ellipse represents the ploughing of the austenitic matrix. (d) SEM micrograph in the backscattered electron (BSE) mode where, the varying contrast between the deformed and undeformed austenite is observed and finally, the two sets of slip planes are indicated in (e).

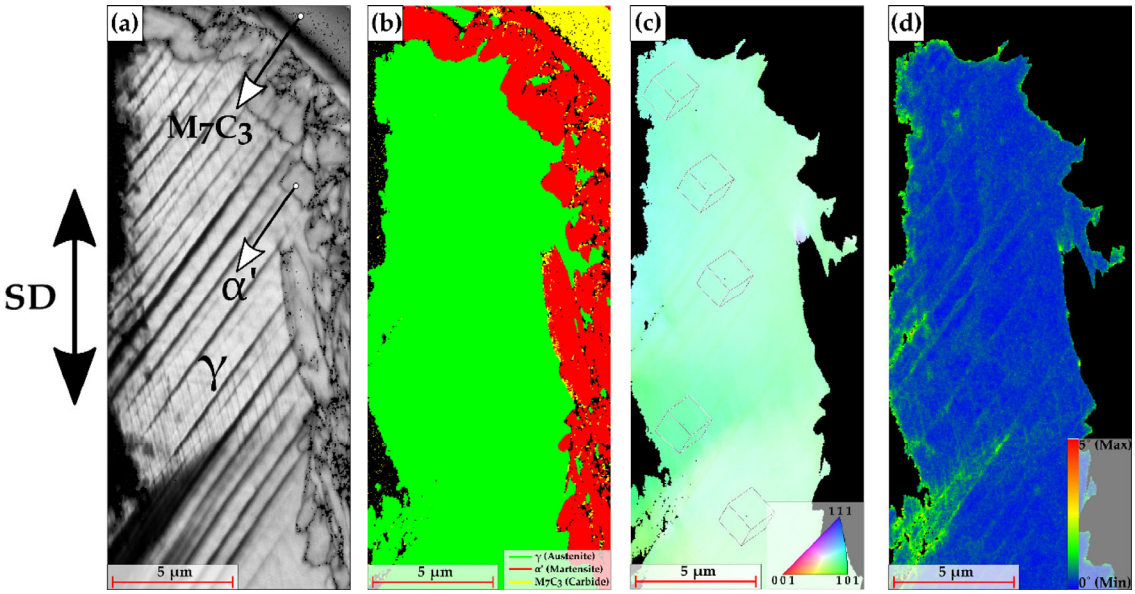

Fig. 6 EBSD measurements on the region adjacent to the 15 N track with (a) IQ map of the scanned region with the respective phases indicated, (b) phase map, with the phases marked in different colours, (c) IPF map of the austenite matrix, overlayed with the local lattice rotation, and (d) KAM map of the austenite matrix.

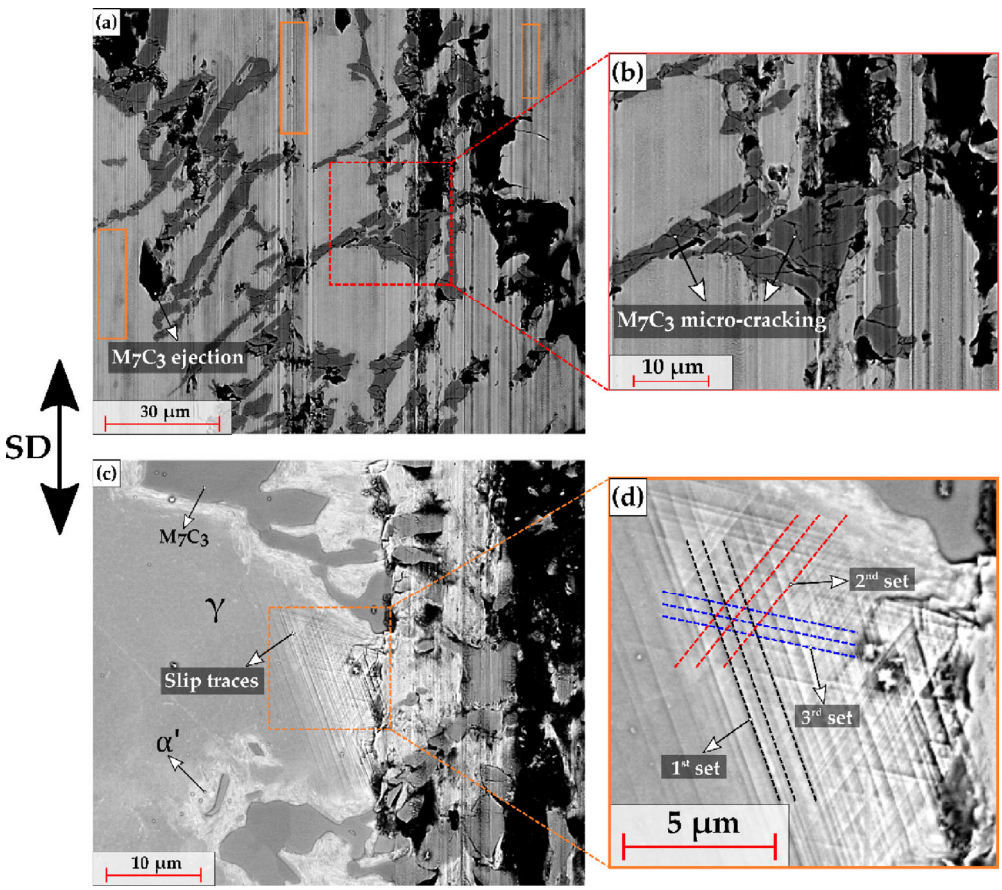

Fig. 7 (a) SEM micrograph in BSE mode of the wear track loaded at 20 N wherein the orange solid rectangle represents the micro-cutting phenomena. The partially cracked and removed carbide is observed in (b). (c) SEM micrograph in the BSE mode where the austenitic matrix (γ), M_7C_3 carbides, martensite phase (α'), and the slip traces are delineated and finally, the three different sets of slip planes are indicated in (d).

and 7(b) that the proportion of cracked and spalled carbides increased compared to the previous loads. Expectedly, in addition to the presence of slip traces, a third set of slip planes was activated, as observed in Fig. 7(c) and marked in Fig. 7(d). The increased load would increase the amount of plastic deformation undergone by the austenitic matrix and thereby, to accommodate the increased dislocation activity, a third set was activated. This third system might have a higher critically resolved shear stress (CRSS) and hence, a larger load was necessary to activate it [54, 55].

Figure 8(a) represents the SEM micrograph of the region adjacent to the wear track where the EBSD measurements were carried out. The IQ map in Fig. 8(b) clearly indicates the variance in the slip band directions, and its consequence is reflected in the IPF map depicted in Fig. 8(d). A variation in the crystal orientation is seen within the austenite, especially at regions where two or even three sets of slip traces intersect, as evident from the crystal lattice rotations in Fig. 8(d). Depending upon the direction of the slip bands with respect to the neighbouring region and the associated strain incompatibilities, a localized lattice rotation occurs within the region [56]. As a result of this, the local misorientation also varies, as observed in the austenite KAM map in Fig. 8(e). Moreover, the difference between the misorientation within the austenite region and the mean orientation was visualized by performing the GROD measurements, as represented in Fig. 8(f). A clear orientational difference between the austenitic region bordering the wear track and the rest of the austenite can be observed. This was further elucidated by calculating the point-to-point and point-to-origin misorientation profile chart across the austenite grain, as represented in Fig. 8(g). The line profile is marked in Fig. 8(f) as the horizontal white dashed line. Clearly, while crossing over the point at approximately 2 μm from the origin, a spike can be seen in the blue curve, which indicates the orientational difference. Furthermore, the point-to-origin curve indicates a maximum gradient of about 40° within the austenite region. The different regions within the austenite rotate independently depending on the number of slip systems activated and the direction of the slip bands, to accommodate the imposed plastic strain.

From the SEM micrographs, cracks and grooves were visible on all the worn surfaces. Comparing Fig. 2 with the respective magnified SEM micrographs for all loads, it was evident that the wear mechanism was a combination of both adhesive and abrasive wear. At loads below P_C, adhesion was the dominant wear mechanism with signs of mild abrasion, but at loads equal to and above P_C, a shift was observed with the dominant wear mechanism being abrasion. Given the inherent ductility of the austenitic matrix, micro-ploughing ensued whereas micro-cutting affected the harder, more brittle M_7C_3 EC, owing to its inability to plastically deform. The M_7C_3 carbides had cracked and fractured owing to the higher hardness of the abrasive, and the inability of the hardened austenitic matrix in adequately providing the necessary mechanical support resulted in its spallation. The spallation of carbides results in the formation of voids that can act as a reservoir to trap the particles generated during the wear process, potentially altering the wear behaviour during sliding [57, 58]. Moreover, the cracked carbide could act as a third body which can affect other carbides as well, leading to the formation of grooves in the leading edge of the carbide during abrasion [23, 59]. Therefore, the likelihood for micro-cutting increased with increasing load and it could be attributed to the higher propensity for carbide spallation combined with the increased rate at which the austenite plastically deforms. As the micro-cutting mechanism causes a greater loss in the material [10, 60], and given its proclivity with increasing load, it could be postulated that a higher volume loss can be expected.

Furthermore, the increased rate of the strain hardening of the austenitic matrix was reflected in the hardness values that were measured vicinal to the wear track, as indicated in Table 4. Compared to the hardness value of the undeformed austenitic matrix, an increase in the matrix hardness was observed at regions adjacent to the wear track and as the load increased, the average hardness value increased as well. This was attributable to the increase in the dislocation activity within the austenite leading to the activation of multiple slip systems and increased strain hardening, and subsequently, a higher hardness.

In addition to the oxide-based counter-body used in the current study, given the environmental conditions of testing (25 °C and 45% humidity), there

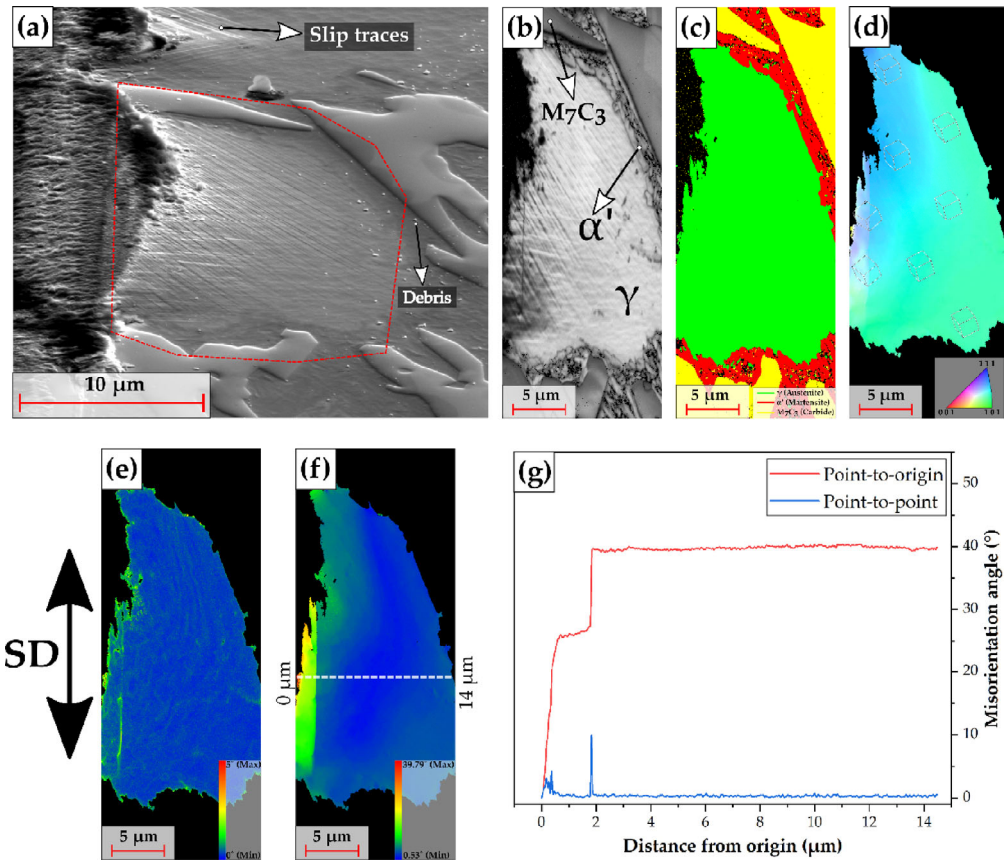

Fig. 8 (a) SEM SE micrograph of the region adjacent to the 20 N wear track where the slip traces and wear debris are marked for reference. The red dashed enclosure in (a) represents the area where the EBSD measurements were carried out, with (b) IQ map of the scanned region with the respective phases indicated, (c) phase map with the phases marked in different colours, (d) IPF map of the austenite matrix, overlayed with the local lattice rotation, (e) KAM map of the austenite matrix, and (f) GROD map of the austenite matrix. The variation of the misorientation angle across the austenite grain, following a path (0 → 14 μm) indicated by the dashed white line in (f), is graphically represented in (g).

Table 4 Matrix hardness adjacent to the wear tracks for the different loads.

Undeformed matrix hardness	Matrix hardness adjacent to wear track		
	5 N	15 N	20 N
336 ± 6	354 ± 7	375 ± 7	406 ± 19

is a high tendency for oxidation to occur [61]. This can be qualitatively appreciated in the EDS measurements. Figure 9(a) represents the SEM micrograph with a 50% overlay of the oxygen EDS concentration map for the wear track loaded at 20 N. It indicates the preferential accumulation of oxides at areas where the carbides were cracked and spalled. As the wear mechanism is abrasion-dominated, micro-cutting and ploughing contribute to surface deterioration resulting in the generation of numerous defects such as cracks and voids. This is a crucial factor to consider, as the rate of carbide removal essentially indicates the rate at which the oxides accumulate and eventually breakdown, altering the subsequent wear behaviour [37]. Additionally, Fig. 9(b) represents a closer view of the oxide accumulation at the location where the M_7C_3 carbide was ejected and from the elemental EDS concentration maps (Figs. 9(c)–9(e)), it can be deduced that oxide formed is iron-chromium oxide.

Another important aspect to take into consideration is the temperature rise at the contact interface (i.e., flash temperature) between the ball and the sample surface, as it could engender structural changes and/or phase transformations [59]. The flash temperature

was previously estimated by several researchers who demonstrated that under similar conditions, the rise in temperature was not significant [62–65]. Nevertheless, the peak flash temperature was calculated for the current study, based on the equations provided in Ref. [27] and it yielded a value of 17 K for the maximum load (20 N). This value can be considered very minimal for any thermally induced structural changes and/or phase transformations to occur [66].

Therefore, it can be conclusively stated that the thermal effects emanating during the dry sliding tests are negligible and the microstructural changes occurring around the wear track are predominately mechanically induced. It is also worth to note that as the diffusivity of oxygen is faster under mechanically driven conditions, oxidation is favoured [61, 67].

To observe the deformed microstructure directly beneath the wear track, transverse cuts were made across the track to obtain the desired cross-sections. Prior to cutting, the sample surface was protected by electrolytically coating it with Ni. The evaluation of the deformed microstructure and deformation depth, especially under the centre of the track would be beneficial for further analysis, as the maximum stress is experienced at the centre of the wear track width [57, 65].

Figure 10 represents the cross-section microstructure of the sample after subjecting it to sliding at the maximum load (20 N). It was observed that the EC closer to the worn surface had broken whereas the EC located further below are intact despite belonging to the same EC, as indicated in the orange dashed ellipse. Nevertheless, the presence of the uniformly coated Ni layer protected the carbides from ejection during the mechanical cross-sectioning and preparation.

The extent of deformation depth was visualized with the help of EBSD measurements. Figure 11(a) represents the SEM micrograph of the area underneath the wear track loaded at 20 N and Fig. 11(b) focuses on the area considered for the EBSD measurements. The scanned area was 10 μm × 120 μm. In addition to the IQ and the phase map, GROD analysis of the austenitic regions was carried out to obtain the variation in orientation within each grain with increasing cross-sectional depth, as represented in Fig. 11(e). Moreover, considering the undeformed austenite as the starting point, point-to-origin misorientation graph was plotted, as shown in Fig. 11(f).

The GROD maps in Fig. 11(e) clearly indicate the evolution of the microstructure directly beneath the wear surface. It starts with an increase in the misorientations within the grain and presence of slip bands as seen from the IQ maps. The austenite grain has clearly undergone plastic deformation owing to the stress exerted on it and moreover, it has extended across the carbide, towards the austenite grain located below. Comparing Fig. 10 with the IQ map in Fig. 11(c), it can be assessed that even though the eutectic carbides are broken, they are fairly supported by the highly dislocated austenitic matrix.

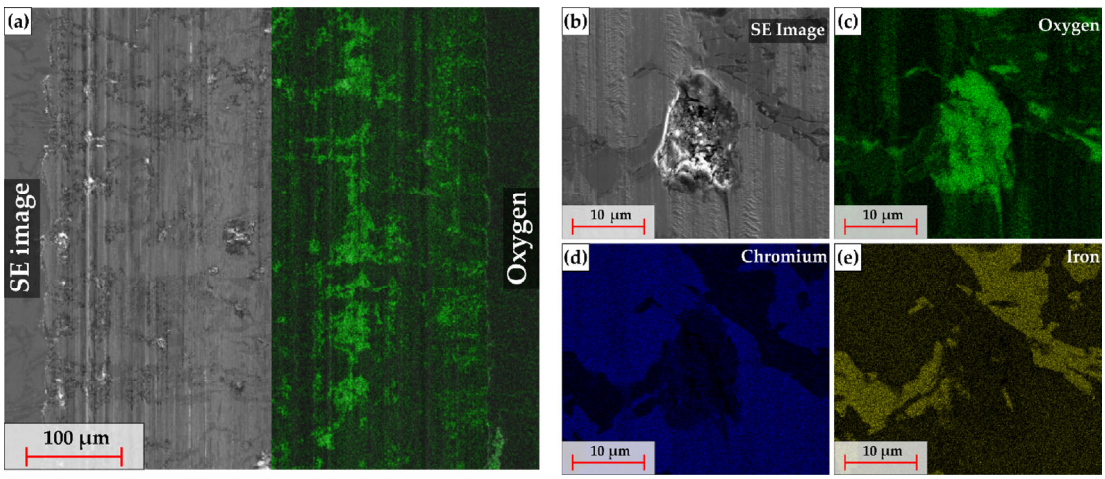

Fig. 9 (a) SEM micrograph in SE mode, with a 50% overlay of the oxygen EDS concentration map. The SEM SE micrograph of a magnified region in the wear track is represented in (b) whereas, the EDS concentration maps pertaining to oxygen, chromium, and iron, are indicated in (c), (d), and (e), respectively.

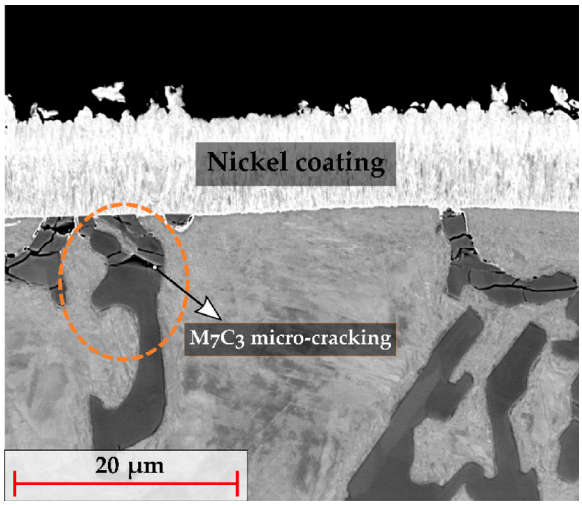

Fig. 10 Representative SEM micrograph in BSE mode of the cross section of the worn sample coated with Ni and loaded at 20 N. The orange dashed ellipse represents the carbide micro-cracking.

The point-to-origin misorientation plot indicates a maximum misorientation of about 13°, between the undeformed austenite and the austenite that was heavily deformed. As the strain experienced by the austenite decreases with increasing depth, from the above measurements, the deformation depth was estimated to be about 40 μm.

Additionally, the hardness of the austenitic matrix with increasing cross-sectional depth was measured using the Vickers method and is graphically represented in Fig. 12. An exponential decrease in hardness with increasing distance from the wear surface was seen. Likewise, it was observed that the matrix hardness rapidly approaches the mean undeformed matrix hardness after about 40 μm from the wear surface. This further signifies that the deformation depth is around 40 μm under the wear track loaded with 20 N.

In addition to the ability of the austenitic matrix to plastically deform owing to the dislocation interactions, its ability to transform to martensite (SIM) during service is also thought to contribute to the work hardening behaviour [37]. Nevertheless, the EBSD measurements on the wear track loaded maximally (20 N), did not show the presence of SIM at the deformed zone, adjacent (Fig. 8) or under the wear track (Fig. 11). This could be attributable to two reasons: (1) low strain rate in the present study and (2) the absence of shear band intersections, which act as potential nucleating sites for SIM formation [66, 68, 69]. In fact, the formation of shear bands in the microstructure usually stems from application of high strain rates which lead to local plastic instability. They are narrow regions of intense shear, resulting in inhomogeneous deformation, possessing orientations that are quite different from the parent matrix orientation [70]. Additionally, EBSD scanning over areas consisting of shear bands would lead to 'black

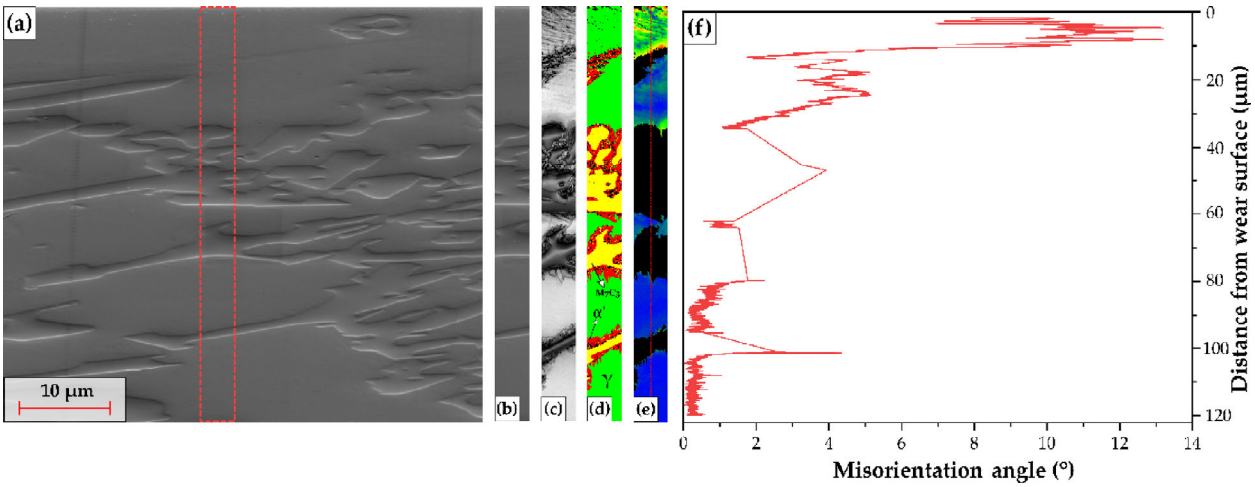

Fig. 11 (a) SEM micrograph in the SE mode of the area beneath the wear track loaded at 20 N, with the red dashed rectangle indicating the region (10 μm × 120 μm) considered for the EBSD measurements, as seen in (b). The IQ map of the scanned region is indicated in (c) whereas (d) represents the phase map, with the respective phases marked. The GROD maps of only the austenite regions are represented in (e). The red dashed vertical line within (e) indicates the line profile followed to obtain the misorientation angle as a function of the distance from the wear surface, as graphically represented in (f).

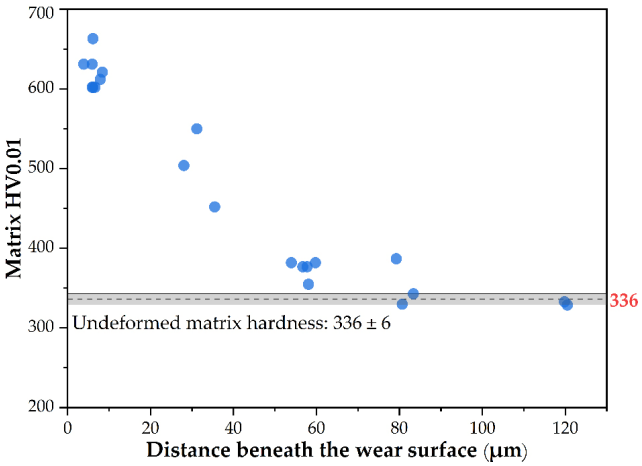

Fig. 12 Variation of matrix hardness with increasing distance from the surface of the wear track, loaded at 20 N.

spots' which is categorized as unable-to-index pixels [60].

In the current study, the formed 'lines' adjacent and underneath the wear track were inferred as slip traces based on the minimal orientation change between the slip band boundary and the austenitic matrix, as evidenced by EBSD. Moreover, it was possible to index the entire region that included the slip bands.

3.2 Wear rate and friction behaviour

The average wear volume (mm^3) calculated using the LEXT software and the wear rate, computed using Eq. (3), for each load is presented in Fig. 13. As expected, increasing the load led to an increase in the wear volume and consequently, the wear rate.

The increased load led to increased plastic deformation, dislocation activity, and the subsequent

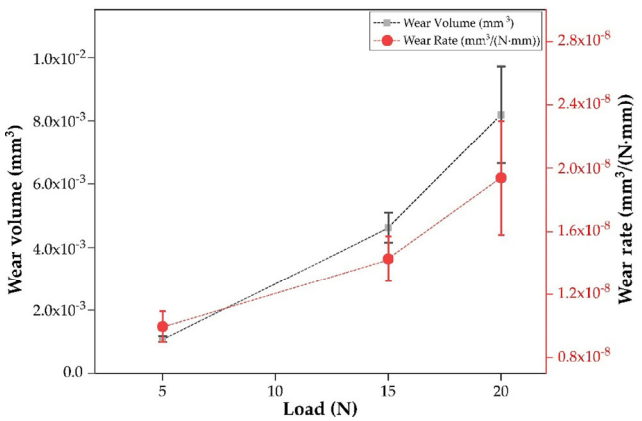

Fig. 13 Average wear volume and wear rate for each load.

activation of multiple slip systems resulting in a harder austenitic matrix, as evidenced from the hardness values adjacent to the wear track. Moreover, given that the hardness of the counter-body used is higher than the M_7C_3 EC, carbide micro-cracking ensued, leading to eventual ejection from the surface [25, 26]. This, in conjunction with the inability of the deformed, harder austenitic matrix to mechanically support the broken carbide fragments proved deleterious thereby, increasing the wear rate of the system. Furthermore, the oxidation taking place at the contact surface, preferentially accumulating at areas where the carbides have been removed, can also lead to increased wear activity, owing to its inherent brittleness.

The frictional behaviour of the samples under varying loads is expressed in terms of COF. The mean COF was plotted for each load and is represented in Fig. 14. In all cases, the curves initially rose quickly to reach a peak (running-in), before decreasing and reaching a steady state behaviour. The COF development within the first 100–200 cycles is similar for all cases, resembling a type b curve from those shown by Blau, which is a characteristic of non-lubricated dry metallic sliding systems [71]. This evolution is characterized by the removal of the initial asperities of both contact bodies, which results in higher local contact pressures and consequently, higher friction. The running-in behaviour could be further explained by the surface compositional changes caused due to the sliding action between the ball and the sample surface [52, 71]. Once conformality is achieved, the COF is settled at its steady state value. It is also interesting to note that the running-in and steady state behaviour is achieved earlier for the 5 N compared to the other loads and this can be due to the lower damage sustained by the ball thereby, establishing a stable contact faster. With increased load, the contact radius increases, and more dynamic processes transpire leading to a delay in reaching steady state. Nevertheless, the steady state COF is observed to be about 0.4 in all cases. In the case of the 20 N sample, stronger COF fluctuations are observed during the steady state. This might be related to the heterogeneity of the contact interface (Figs. 1(b) and 1(c)), consisting of a larger amount of the matrix and the carbides, which destabilize the COF development [72].

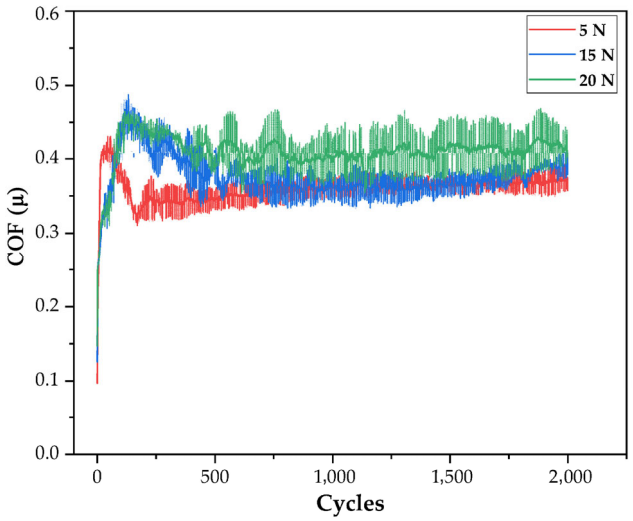

Fig. 14 Evolution of COF with increasing cycles for the differently loaded wear samples.

In both Figs. 13 and 14, the standard deviations pertaining to 20 N are more spread out. Given the increased propensity for carbide cracking, an oxide layer is formed (as suggested from Figs. 9(a) and 9(c)), which temporally increases in thickness until reaching a critical value. Upon reaching a critical thickness value, the shear stresses exerted during the wear is large enough to cause film rupture. This process continues, inducing a dynamic cycle of oxide layer formation and breakage [72]. The ensuing breakage also aids in the formation of wear debris which is visible in the SEM micrographs. Moreover, the geometrical orientation of the EC with respect to the sliding direction could also play a crucial role.

4 Conclusions

In the current study, dry-sliding linear reciprocating tribological tests were performed on a 26% Cr as-cast HCCI alloy with varying loads. The influence of increasing the load on the matrix microstructural evolution and the subsequent wear behaviour of the alloy was examined and the following conclusions were drawn.

1) The determination of P_C by analytical calculations were in accordance with the microstructural observations carried out using SEM. No evidence of plastic deformation of the austenitic matrix adjacent to the wear track was observed for 5 N, whereas the wear tracks loaded with 15 and 20 N showed the presence of slip traces (evidence of plastic deformation). Moreover, the number of activated slip systems increased with increasing load.

2) The deformation of the austenitic matrix beneath the wear track was successfully visualized using electron backscattered diffraction (EBSD). Grain reference orientation deviation (GROD) and image quality (IQ) maps indicated a decrease in the misorientation and deformation, respectively, with increasing depth.

3) At loads below P_C, adhesion was the dominant wear mechanism with signs of mild abrasion, but at loads equal to and above P_C, a shift was observed with the dominant wear mechanism being abrasion. The increased tendency for spalling combined with the strain hardening proclivity of the austenitic matrix led to poor mechanical stability being imparted.

4) The shift in the dominant wear mechanism was also reflected in the wear volume and the wear rate, which increased with increasing load.

5) The running-in and steady state behaviour is achieved earlier for samples tested with 5 N, compared to the other loads. This can be attributed to the stable contact established by the lower load, and the increased tendency for plastic deformation and associated effects at higher loads.

To sum up, Hertzian contact theory was used to determine the critical load based on the materials' properties and accordingly, the loads were defined. The calculated values were in good correspondence with the microstructural and/or morphological observations. Moreover, a clear shift in the dominant wear mechanism was identified owing to the behaviour of the austenitic matrix and the carbide during the wear process. Consequently, this methodology can be further extended to other alloys in the high chromium cast iron (HCCI) family to establish the load limits and to better understand the interaction between the different components in the system.

Acknowledgements

The present work is supported by funding from the Deutsche Forschungsgemeinschaft (DFG, project: GU 2102/2-1). The authors would like to thank Martin

Duarte from Tubacero S.A. for providing the materials, and Prof. Christian Motz for granting access to perform nanoindentation measurements. Additionally, U.P.N. is grateful to DAAD for the financial support.

References

[1] Tabrett C P, Sare I R, Ghomashchi M R. Microstructure-property relationships in high chromium white iron alloys. *Int Mater Rev* **41**(2): 59–82 (1996)

[2] ASTM International. Standard Specification for Abrasion Resistance Cast Irons: ASTM Standard A 532/A 532M-93a. West Conshohocken, PA, USA, 2003

[3] Xu H, Xu Y, He Y, et al. Two-stage warm cross rolling and its effect on the microstructure, texture and magnetic properties of an Fe-6.5 wt% Si non-oriented electrical steel. *J Mater Sci* **55**(26): 12525–12543 (2020)

[4] Maratray F. Choice of appropriate compositions for chromium-molybdenum white irons. *AFS Trans* **79**: 121–124 (1971)

[5] Llewellyn R J, Yick S K, Dolman K F. Scouring erosion resistance of metallic materials used in slurry pump service. *Wear* **256**(6): 592–599 (2004)

[6] Karantzalis E, Lekatou A, Mavros H. Microstructure and properties of high chromium cast irons: Effect of heat treatments and alloying additions. *Int J Cast Met Res* **22**(6): 448–456 (2009)

[7] Wiengmoon A, Pearce J T H, Chairuangsri T. Relationship between microstructure, hardness and corrosion resistance in 20 wt%Cr, 27 wt%Cr, and 36 wt%Cr high chromium cast irons. *Mater Chem Phys* **125**(3): 739–748 (2011)

[8] Rivlin V G. 14: Critical review of constitution of carbon–chromium–iron and carbon–iron–manganese systems. *Int Met Rev* **29**(1): 299–327 (1984)

[9] Maratray F, Usseglio-Nanot R. Factors affecting the structure of chromium and chromium-molybdenum white irons. *Climax Molybdenum SA*, 1971: 1–32

[10] Pearce J T H. Structure and wear performance of abrasion resistance chromium white cast irons. *Trans Am Foundrymen's Soc* **92**: 599–622 (1984)

[11] Wiengmoon A. Carbides in high chromium cast irons. *Naresuan Univ Eng J* **6**(1): 64–70 (2011)

[12] Doğan Ö N, Hawk J A. Effect of carbide orientation on abrasion of high Cr white cast iron. *Wear* **189**(1–2): 136–142 (1995)

[13] Fulcher J K, Kosel T H, Fiore N F. The effect of carbide volume fraction on the low stress abrasion resistance of high Cr–Mo white cast irons. *Wear* **84**(3): 313–25 (1983)

[14] Bedolla-Jacuinde A, Correa R, Mejía I, Quezada J G, Rainforth W M. The effect of titanium on the wear behaviour of a 16%Cr white cast iron under pure sliding. *Wear* **263**(1–6): 808–820 (2007)

[15] Bedolla-Jacuinde A, Guerra F V., Mejía I, Zuno-Silva J, Rainforth M. Abrasive wear of V–Nb–Ti alloyed high-chromium white irons. *Wear* **332**–**333**: 1006–1011 (2015)

[16] Correa R, Bedolla-Jacuinde A, Zuno-Silva J, Cardoso E, Mejía I. Effect of boron on the sliding wear of directionally solidified high-chromium white irons. *Wear* **267**(1–4): 495–504 (2009)

[17] Cortés-Carrillo E, Bedolla-Jacuinde A, Mejía I, Zepeda C M, Zuno-Silva J, Guerra-Lopez F V. Effects of tungsten on the microstructure and on the abrasive wear behavior of a high-chromium white iron. *Wear* **376**–**377**: 77–85 (2017)

[18] Archard J F. Contact and rubbing of flat surfaces. *J Appl Phys* **24**(8): 981–988 (1953)

[19] Zum Gahr K H, Doane D V. Optimizing fracture toughness and abrasion resistance in white cast irons. *Metall Trans A* **11**(4): 613–620 (1980)

[20] Asensio J, Pero-Sanz J A, Verdeja J I. Microstructure selection criteria for cast irons with more than 10 wt% chromium for wear applications. *Mater Charact* **49**(2): 83–93 (2002)

[21] Laird G, Gundlach R, Rohrig K. *Abrasion-resistant Cast Iron Handbook*. Schaumburg (USA): American Foundry Society, 2000.

[22] Avery H S. The measurement of wear resistance. *Wear* **4**(6): 427–449 (1961)

[23] Doğan Ö N, Hawk J A, Laird G. Solidification structure and abrasion resistance of high chromium white irons. *Metall Mater Trans A Phys Metall Mater Sci* **28**(6): 1315–1328 (1997)

[24] Turenne S, Lavallée F, Masounave J. Matrix microstructure effect on the abrasion wear resistance of high-chromium white cast iron. *J Mater Sci* **24**(8): 3021–3028 (1989)

[25] Gundlach R B, Parks J L. Influence of abrasive hardness on the wear resistance of high chromium irons. *Wear* **46**(1): 97–108 (1978)

[26] Zum Gahr K H, Eldis G T. Abrasive wear of white cast irons. *Wear* **64**(1): 175–194 (1980)
[27] Hutchings I M. *Tribology: Friction and Wear of Engineering Materials*. Oxford (UK): Butterworth-Heinemann, 1992.
[28] Porter D A, Easterling K E, Sherif M Y. *Phase Transformations in Metals and Alloys*. Boca Raton (USA): CRC Press, 2009.
[29] Tabrett C P, Sare I R. Effect of high temperature and sub-ambient treatments on the matrix structure and abrasion resistance of a high-chromium white iron. *Scr Mater* **38**(12): 1747–1753 (1998)
[30] Higuera-cobos O F, Dumitru F-D, Mesa-Grajales D H. Improvement of abrasive wear resistance of the high chromium cast iron ASTM A-532 through thermal treatment cycles. *Rev Fac Ing* **25**(41): 93–103 (2015)
[31] Guitar M A, Suárez S, Prat O, Duarte Guigou M, Gari V, Pereira G, et al. High chromium cast irons: Destabilized-subcritical secondary carbide precipitation and its effect on hardness and wear properties. *J Mater Eng Perform* **27**(8): 3877–3885 (2018)
[32] Inthidech S, Kosasu P, Yotee S, Matsubara Y. Effect of repeated tempering on abrasive wear behavior of hypoeutectic 16 mass% Cr cast iron with molybdenum. *Mater Trans* **54**(1): 28–35 (2013)
[33] Abdel-Aziz K, El-Shennawy M, Omar A A. Microstructural characteristics and mechanical properties of heat treated high-cr white cast iron alloys. *Int J Appl Eng Res* **12**(14): 4675–4686 (2017)
[34] Watson J D, Mutton P J, Sare I R. Abrasive wear of white cast irons. *Met forum* **3**(1): 74–88 (1980)
[35] Scandian C, Boher C, de Mello J D B, Rézaï-Aria F. Effect of molybdenum and chromium contents in sliding wear of high-chromium white cast iron: The relationship between microstructure and wear. *Wear* **267**(1–4): 401–408 (2009)
[36] Pintaude G, Bernardes F G, Santos M M, Sinatora A, Albertin E. Mild and severe wear of steels and cast irons in sliding abrasion. *Wear* **267**(1–4): 19–25 (2009)
[37] Bedolla-Jacuinde A, Rainforth W M. Electron microscopy analysis on the worn surface of a high-chromium white iron during dry sliding contact. *Mater Res Soc Symp Proc* **843**: 299–304 (2005)
[38] Pokusová M, Berta I, Šooš Ľ. Abrasion resistance of as-cast high-chromium cast iron. *Sci Proc* **22**(1): 74–79 (2014)
[39] Nayak U P, Guitar M A, Mücklich F. A comparative study on the influence of chromium on the phase fraction and elemental distribution in as-cast high chromium cast irons: Simulation vs. experimentation. *Metals (Basel)* **10**(1): 30 (2020)
[40] Nayak U P, Guitar M A, Mücklich F. Evaluation of etching process parameter optimization in the objective specific microstructural characterization of as-cast and heat treated HCCI alloy. *Prakt Metallogr* **57**(10): 688–713 (2020)
[41] Laird G, Powell G L F. Solidification and solid-state transformation mechanisms in Si alloyed high-chromium white cast irons. *Metall Trans A* **24**(4): 981–988 (1993)
[42] Carpenter S D, Carpenter D, Pearce J T H. XRD and electron microscope study of an as-cast 26.6% chromium white iron microstructure. *Mater Chem Phys* **85**(1): 32–40 (2004)
[43] Greenwood J A, Williamson J B P. Contact of nominally flat surfaces. *Proc R Soc London A* **295**(1442): 300–319 (1966)
[44] Jackson R L, Green I. A finite element study of elasto-plastic hemispherical contact against a rigid flat. *J Tribol* **127**(2): 343–354 (2005)
[45] Tabor D. *The Hardness of Metals*. Oxford (UK): Claredon Press, 1951.
[46] Kugel Pompel. Datenblatt Data sheet, https://www.kugelpompel.at/de/Prazisionskugeln/kugeln/aluminiumoxydkeramikkugel-3000-mm-g28, 2020.
[47] Auerkari P. Mechanical and physical properties of engineering alumina ceramics. Technical Research Centre of Finland, Espoo, Finland, 1996: 26.
[48] ASM International. ASM Handbook: Properties and Aelection: Irons, Steels, and High Performance Alloys. Novelty (USA): ASM International, 2001.
[49] Rabinowicz E, Dunn L A, Russell P G. A study of abrasive wear under three-body conditions. *Wear* **4**(5): 345–355 (1961)
[50] Atabaki M M, Jafari S, Abdollah-pour H. Abrasive wear behavior of high chromium cast iron and hadfield steel—A comparison. *J Iron Steel Res Int* **19**(4): 43–50 (2012)
[51] Penagos J J, Pereira J I, Machado P C, Albertin E, Sinatora A. Synergetic effect of niobium and molybdenum on abrasion resistance of high chromium cast irons. *Wear* **376–377**: 983–992 (2017)
[52] Hurricks P L. Some Metallurgical Factors Controlling the adhesive and abrasive wear resistance of steels: A review. *Wear* **26**: 285–301 (1973)
[53] Schwartz A J, Kumar M, Adams B L, Field D P. *Electron Backscatter Diffraction in Materials Science*. Boston (USA): Springer US, 2009.
[54] Reza Abbaschian, Abbaschian L, Reed-Hill R E. *Physical Metallurgy Principles*. Stamford (USA): Cengage Learning, 2008.
[55] Hull D, Bacon D J. *Introduction to Dislocations*. Oxford (UK): Elsevier Ltd., 2011.
[56] Di Gioacchino F, Quinta Da Fonseca J. An experimental study of the polycrystalline plasticity of austenitic stainless steel. *Int J Plast* **74**: 92–109 (2015)
[57] Menezes P L, Ingole S P, Nosonovsky M, Kailas S V., Lovell M R. *Tribology for Scientists and Engineers: From Basics to Advanced Concepts*. New York (USA): Springer-Verlag New York, 2013.
[58] Ghabchi A. Wear resistant carbide-based thermal sprayed coatings: Process, properties, mechanical degradation and wear. Ph.D. Thesis. New York (USA): Stony Brook University, 2011.
[59] Chen L, Persson J, Ståhl J E, Zhou J M. Nano-scratching resistance of high-chromium white cast iron and its correlation with wear of cBN tool in machining. *J Superhard Mater* **39**(5): 365–372 (2017)

[60] Kazemipour M, Shokrollahi H, Sharafi S. The influence of the matrix microstructure on abrasive wear resistance of heat-treated Fe–32Cr–4.5C wt% hardfacing alloy. *Tribol Lett* **39**(2): 181–192 (2010)
[61] Sullivan J L, Quinn T F J, Rowson D M. Developments in the oxidational theory of mild wear. *Tribol Int* **13**(4): 153–158 (1980)
[62] So H, Yu D S, Chuang C Y. Formation and wear mechanism of tribo-oxides and the regime of oxidational wear of steel. *Wear* **253**(9–10): 1004–1015 (2002)
[63] Ashby M F, Abulawi J, Kong H S. Temperature maps for frictional heating in dry sliding. *Tribol Trans* **34**(4): 577–582 (1991)
[64] Lingard S. Estimation of flash temperatures in dry sliding. *Proc Inst Mech Eng Part C J Mech Eng Sci* **198**(2): 91–97 (1984)
[65] Grützmacher P G, Rammacher S, Rathmann D, Motz C, Mücklich F, Suarez S. Interplay between microstructural evolution and tribo-chemistry during dry sliding of metals. *Friction* **7**(6): 637–650 (2019)
[66] Levitas V I, Idesman A V, Olson G B. Continuum modeling of strain-induced martensitic transformation at shear-band intersections. *Acta Mater* **47**(1): 219–233 (1998)
[67] Rigney D A. Transfer, mixing and associated chemical and mechanical processes during the sliding of ductile materials. *Wear* **245**(1–2): 1–9 (2000)
[68] Talonen J, Hänninen H. Formation of shear bands and strain-induced martensite during plastic deformation of metastable austenitic stainless steels. *Acta Mater* **55**(18): 6108–618 (2007)
[69] Mao B, Chu S, Wang S. Effect of grain size on the friction-induced martensitic transformation and tribological properties of 304 austenite stainless steel. *Metals (Basel)* **10**(9): 1–14 (2020)
[70] Gottstein G. *Physical Foundations of Materials Science*. Berlin (Germany): Springer Berlin Heidelberg, 2004.
[71] Blau P J. Interpretations of the friction and wear break-in behavior of metals in sliding contact. *Wear* **71**(1): 29–43 (1981)
[72] Blau P J. On the nature of running-in. *Tribol Int* **38**(11–12): 1007–1012 (2005)

U. Pranav NAYAK. He received his B.Tech. degree in metallurgical and materials engineering in 2014 from the National Institute of Technology Karnataka (NITK), Mangalore, India. He obtained his M.Sc. degree in materials science under the Erasmus Mundus FAME Program in 2016. Since 2018, he is a doctoral candidate at the Chair of Functional Materials (Saarland University) with his research focusing on the microstructure tailoring in high chromium cast iron (HCCI) alloys through heat treatment design.

María Agustina GUITAR. She received her electromechanical engineering degree in 2005 from the National Technical University in Argentina, her master degree in materials science in 2007 from the National University of San Martin in Argentina, and her Ph.D. degree in materials science and engineering in 2014 from Saarland University, Germany. She currently leads the Steel and Ferrous-based Materials Group at the Chair of Functional Materials (Saarland University). Her research focuses in tailoring the microstructure of high chromium cast irons for performance optimization.